

C₆₀-based ionic salt electron shuttle for high-performance inverted perovskite solar modules

Shuai You,^{1#} Hongwei Zhu,^{2#} Zhongjin Shen,^{3#} Xiaoming Wang,⁴ Bingyao Shao,² Qingxiao Wang,⁵ Jianxun Lu,² Youyou Yuan,⁵ Benjia Dak Dou,⁶ Erin M. Sanhira,⁶ Todd Russell,⁶ Adam Lorenz,⁶ Yifan Dong,¹ Lei Chen,¹ Marco Casareto,⁷ Nicholas Rolston,⁷ Matthew C. Beard,¹ Joseph J. Berry,^{8,9,10} Marina Freitag,^{3*} Yanfa Yan,^{4*} Osman M. Bakr,^{2*} Kai Zhu^{1*}

¹ Chemistry and Nanoscience Center, National Renewable Energy Laboratory, Golden, CO, 80401, USA

² Division of Physical Science and Engineering, Center for Renewable Energy and Storage Technologies (CREST), King Abdullah University of Science and Technology, Thuwal, 23955-6900, Saudi Arabia

³ School of Natural and Environmental Sciences, Newcastle University, Newcastle upon Tyne, NE1 7RU, United Kingdom

⁴ Department of Physics and Astronomy and Wright Center for Photovoltaics Innovation and Commercialization, The University of Toledo, Toledo, OH, 43606, USA

⁵ Imaging and Characterization Core Lab, King Abdullah University of Science and Technology, Thuwal, 23955-6900, Saudi Arabia

⁶ CubicPV Inc., 28 Crosby Dr Unit 2500, Bedford, MA, USA

⁷ School of Electrical, Computer and Energy Engineering, Arizona State University, Tempe, AZ, 85281 USA

⁸ Materials Science Center, National Renewable Energy Laboratory, Golden, CO, 80401, USA

⁹ Renewable and Sustainable Energy Institute, University of Colorado Boulder, Boulder, CO, 80309, USA

¹⁰ Department of Physics, University of Colorado Boulder, Boulder, CO, 80309, USA

These authors contributed equally to this work.

* Corresponding authors: kai.zhu@nrel.gov (K.Z.); osman.bakr@kaust.edu.sa (O.M.B); yanfa.yan@utoledo.edu (Y.Yan); marina.freitag@newcastle.ac.uk (M.F.)

Abstract

Although C₆₀ is usually the electron transport layer (ETL) in inverted perovskite solar cells, its molecular nature of C₆₀ leads to weak interfaces that lead to non-ideal interfacial electronic and mechanical degradation. Here, we synthesized an ionic salt from C₆₀, 4-(1',5'-dihydro-1'-methyl-2'H-[5,6] fullereno-C₆₀-I_h-[1,9-c]pyrrol-2'-yl) phenylmethanaminium chloride (CPMAC), and used it as the electron shuttle in inverted PSCs. The CH₂-NH₃⁺ head group in the CPMA cation improved the ETL interface and the ionic nature enhanced the packing, leading to ~3-fold increase in the interfacial toughness compared to C₆₀. Using CPMAC, we obtained ~26% power conversion efficiencies (PCEs) with ~2% degradation after 2,100 hours of 1-sun operation at 65°C. For minimodules (four subcells, 6 centimeters square), we achieved the PCE of ~23% with <9% degradation after 2,200 hours of operation at 55°C.

One-Sentence Summary

Using C₆₀-based ionic salt electron shuttle enhanced the interfacial toughness of the electron transport layer for efficient and stable inverted perovskite solar modules.

Organic-inorganic hybrid metal halide perovskite materials have successfully been used as light absorbers in efficient photovoltaic devices (1-16). The inverted p-i-n perovskite solar cell (PSC) structure is attractive for commercialization because of its easy fabrication, low-temperature processability, and suitability for tandem cells (17-31). The power conversion efficiency (PCE) of single-junction inverted PSCs has exceeded 26% through advances in solvent engineering, compositional tuning, interface optimization, and defect passivation strategies (32-37). However, challenges related to scalability and long-term operational stability are obstacles to their commercialization.

C₆₀ is almost exclusively used in the electron transport layer (ETL) structure for high-performance inverted PSCs, as C₆₀/bathocuproine (BCP) or C₆₀/SnO_x (22). The latter with the SnO_x deposited through atomic layer deposition (ALD) has become the preferred approach for better stability and compatibility with tandems. However, the molecular nature of the C₆₀ layer leads to a weak interface and loose packing, and in turn non-ideal interfacial properties and challenges for ALD-SnO_x coating. These issues inevitably limit the device performance, especially the long-term stability (38-42).

For example, the ALD-SnO_x precursor is known to be reactive with the perovskite surface or even penetrate into the bulk material (43, 44). A C₆₀ layer of around 20 nm (or thicker) is normally needed to support ALD-SnO_x coating (32, 43, 45). Efforts have been made to address the C₆₀/perovskite interface challenges, such as interlayer strategies and C₆₀ functionalization (46-50). However, these strategies focus on perovskite surface defect passivation, interfacial energetics adjustment, or both, whereas the ETLs in these studies still rely on C₆₀ molecules. Thus, these efforts do not address the fundamental issue of the molecular nature of the C₆₀ ETL.

In this study, we use N-methylglycine, and tert-butyl 4-formylbenzylcarbamate molecules and hydrochloric acid to react with C₆₀, to form an ionic salt, 4-(1',5'-dihydro-1'-methyl-2'H-[5,6]fullereno-C₆₀-1h-[1,9-c]pyrrol-2'-yl)phenylmethanaminium chloride (referred to as CPMAC). We further use CPMAC salt as the electron shuttle in inverted PSCs and minimodules. This ionic salt layer fundamentally addressed the disadvantages of molecular C₆₀ layer. Density functional theory

(DFT) calculation revealed that it is energetically preferred for the $\text{CH}_2\text{-NH}_3^+$ heads in the phenylmethanaminium (PMA) units to fill in formamidinium (FA) vacancies or replace FA ions on perovskite surfaces, enabling ionic bonding between CPMA and the perovskite surface. The ionic nature of CPMAC strengthens its interface and packing. The strong electron withdrawing C_{60} unit in the CPMA cation helps ensure the CPMAC is an effective electron conductor. As a result of these physical and chemical characteristics, a thin CPMAC layer was used to support ALD- SnO_x coating to construct an effective ETL. The corresponding PSCs and minimodules using CPMAC show improved PCE and stability compared with those using the conventional C_{60} layers.

Design concept

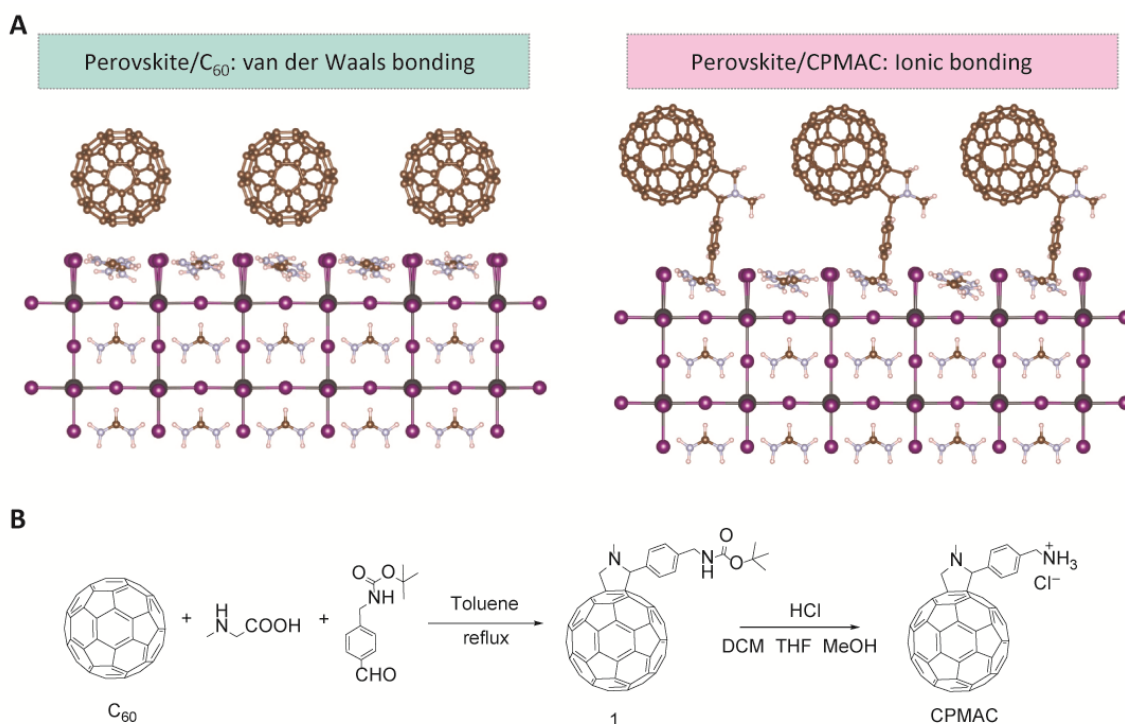


Fig. 1. Design concept. (A) Comparison of C_{60} and CPMAC on their different interactions with the perovskite surface. (B) Synthetic route of 4-(1',5'-dihydro-1'-methyl-2'*H*-[5,6] fullereno- C_{60} -1_{*h*}-[1,9-*c*]pyrrol-2'-yl)phenylmethanaminium chloride (CPMAC).

An ionic salt layer would need the same electron-withdrawing ability but have enhanced ETL interface properties and packing. In our designed CPMAC compound, the CPMA^+ cation

contains a $\text{CH}_2\text{-NH}_3^+$ head with a structure similar to the methylammonium (MA^+) cation. Our DFT calculations showed that CPMAC reaction with FA-rich perovskite surface by replacing an FA^+ cation with CPMA^+ cation lowered the surface energy by 0.375 eV. In comparison, CPMAC reacting with MA^+ would lower surface energy by 0.181 eV, whereas reacting with Cs^+ would increase the surface energy slightly by 0.003 eV. Thus, FA^+ would be replaced preferably by CPMAC for mixed-cation perovskites.

In comparison to C_{60} , two interactions between CPMAC and perovskite were expected. First, the $\text{CH}_2\text{-NH}_3^+$ head could fill a FA^+ vacancy, and the Cl^- anion could occupy an I vacancy, providing double defect passivation. Second, the CPMA^+ cation could replace a FA^+ cation on the surface as expected from our DFT calculation, and FA^+ and Cl^- would form a FACl molecule, which could escape the perovskite during annealing.

A comparison of C_{60} /perovskite and CPMAC/perovskite interfaces is shown in **Fig. 1A**. In both cases (filling a FA^+ vacancy or replacing a FA^+ cation), the $\text{CH}_2\text{-NH}_3^+$ head in the CPMA^+ cation would introduce ionic bonding with the surrounding I anions on the surface. Thus, the ionic nature of CPMAC could strengthen the CPMAC/perovskite interface. It could also enable stronger packing of the CPMAC layer on the perovskite and the use of a thinner CPMAC layer (~ 10 nm) versus ~ 20 nm typically used for C_{60} . In addition, the C_{60} unit in CPMA^+ facilitates electron transport, making the CPMAC layer both a strong and conducting bridge to transfer electrons from the perovskite to external electrodes in a device.

To synthesize CPMAC, we used the Prato reaction of C_{60} with N-methylglycine and tert-butyl 4-formylbenzylcarbamate to form the intermediate (compound **1**), which then reacted with hydrochloric acid in a tert-butyl carbamate deprotection reaction to achieve the final CPMAC compound (**Fig. 1A** and **fig. S1**). Both **1** and final CPMAC compound were characterized by ^1H nuclear magnetic resonance (NMR), ^{13}C NMR, and high-resolution mass spectrometry (**figs. S2 to S5**). Note that the ionic interaction between CPMAC and the perovskite surface is consistent with the x-ray photoelectron spectroscopy (XPS) measurements in which the Pb 4f peaks of the treated perovskite film shifted toward a lower binding energy (by about 0.33 eV) compared to the

control film (**fig. S6**).

Structural and optoelectronic properties

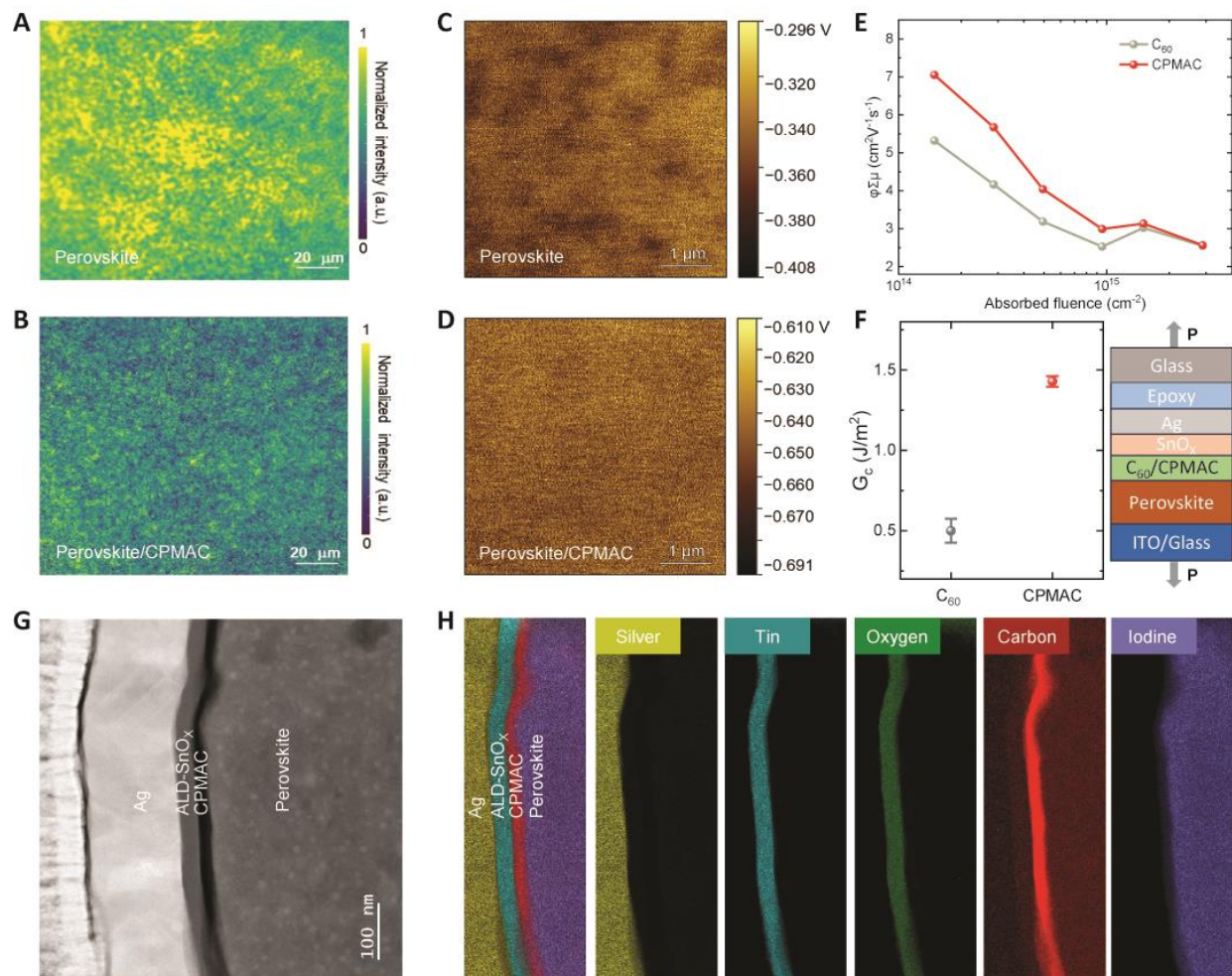


Fig. 2. Structural and optoelectronic properties. (A) and (B) Photoluminescence (PL) imaging of perovskite films without and with CPMAC. (C) and (D) Kelvin probe force microscopy (KPFM) surface potential images for the control and target perovskite films. (E) Comparison of time-resolved microwave conductivity (TRMC) of C₆₀ films and CPMAC films, respectively. (F) Comparison of fracture energy (G_c) of devices to quantify ETL for C₆₀ or CPMAC. (G) Cross-sectional high-angle annular dark-field scanning transmission electron microscopy (HAADF-STEM) images of the Ag/ALD-SnO_x/CPMAC/perovskite. (H) Electron energy loss spectroscopy (EELS) analysis of element mapping for silver (Ag), tin (ALD-SnO_x), oxygen (ALD-SnO_x), carbon (CPMAC), and iodine (perovskite).

We compared the grazing-incident wide-angle x-ray scattering (GIWAXS) studies of the perovskite films without and with CPMAC coating, respectively (**fig. S7**). No additional Laue rings were observed, indicating that the introduction of CPMAC did not induce perovskite phase change. However, the apparent changes in diffraction intensity and growth orientation of the perovskite from the existing Laue rings indicated interactions between CPMAC and the perovskite components. The one-dimensional (1D) GIWAXS results demonstrated a decreased scattering vector q value, corresponding to an increased lattice d -spacing of perovskite (**fig. S7**). These results were consistent with the chemical interaction between CPMAC and perovskite in the surface region.

Photoluminescence (PL) mapping images of perovskite films without and with CPMAC (**Fig. 2, A and B**, respectively) showed that the CPMAC-treated perovskite film was more uniform and has a reduced PL intensity compared to the pristine perovskite film. We used Kelvin probe force microscopy (KPFM) to investigate the spatial variations in the surface potential of perovskite films with and without CPMAC. As shown in **Fig. 2, C and D**, the perovskite/CPMAC film exhibited a more uniform potential distribution than the pristine sample, which suggested that CPMAC effectively mitigates surface defects (51-54). In addition, cyclic voltammetry (CV) measurement of C₆₀ and CPMAC, with ferrocene as the reference, showed lowest unoccupied molecular orbital (LUMO) levels of -4.20 and -4.09 eV against vacuum (**fig. S8**), respectively. In comparison to C₆₀, the reduced conduction band offset between the CPMAC and perovskite (-3.92 eV) should result in a better energy alignment at this interface and a reduced voltage loss in the corresponding device (**fig. S8**).

We measured the time-resolved microwave conductivity (TRMC) transients for both C₆₀ and CPMAC thin films over a range of excitation intensities. The yield-mobility products were plotted as a function of excitation intensities (**Fig. 2E**). The mobility in CPMAC was about 30% higher than that in C₆₀ measured at the lowest excitation intensity.

We further examined the fracture energy (G_C) of devices with C₆₀ or CPMAC by using force-displacement measurements with a double cantilever beam test following a reported

methodology (55). The fracture path of all samples involved the ETL layer and the average G_c values changed by about a factor of 3, increasing from about $0.50 \pm 0.07 \text{ J m}^{-2}$ for C_{60} to $1.43 \pm 0.03 \text{ J m}^{-2}$ for CPMAC (**Fig. 2F**). Glow-discharge optical emission spectroscopy (GDOES) on the delaminated samples further supports the improved fracture toughness within the CPMAC layer as compared to C_{60} as well improved adhesion at the CPMAC/perovskite interface (**fig. S9**). These results were consistent with stronger mechanical stability for CPMAC. These values are above the empirical threshold of 1 J m^{-2} that limits the susceptibility of the perovskite device to delaminate in operation (56).

To directly visualize the distribution of CPMAC on the perovskite layer, we performed high-angle annular dark-field scanning transmission electron microscopy (HAADF-STEM) measurements. Cryogenic focused ion beam (cryo-FIB) was used to prepare the STEM specimen without damaging the inherent structures of the perovskite layer. The cross-sectional HAADF-STEM images in **Fig. 2G** revealed a dark layer sandwiched between the brighter ALD- SnO_x and perovskite layers. This layer corresponded to the CPMAC layer and is discernible because of the contrast in atomic number. The CPMAC layer is $\sim 10 \text{ nm}$ thick and is amorphous (**fig. S10**). To further investigate the elemental distribution, we performed electron energy loss spectroscopy (EELS) coupled with cryogenic-high-resolution transmission electron microscopy (cryo-HRTEM) experiments on cross sections of the device (**Fig. 2H**). The distributions of silver, tin, oxygen, carbon, and iodine were consistent with the distributions of the Ag, ALD- SnO_x , ALD- SnO_x , CPMAC, and perovskite layers. EELS also revealed the uniform and compact presence of the CPMAC layer atop perovskite through the detection of the carbon element.

Device characteristics

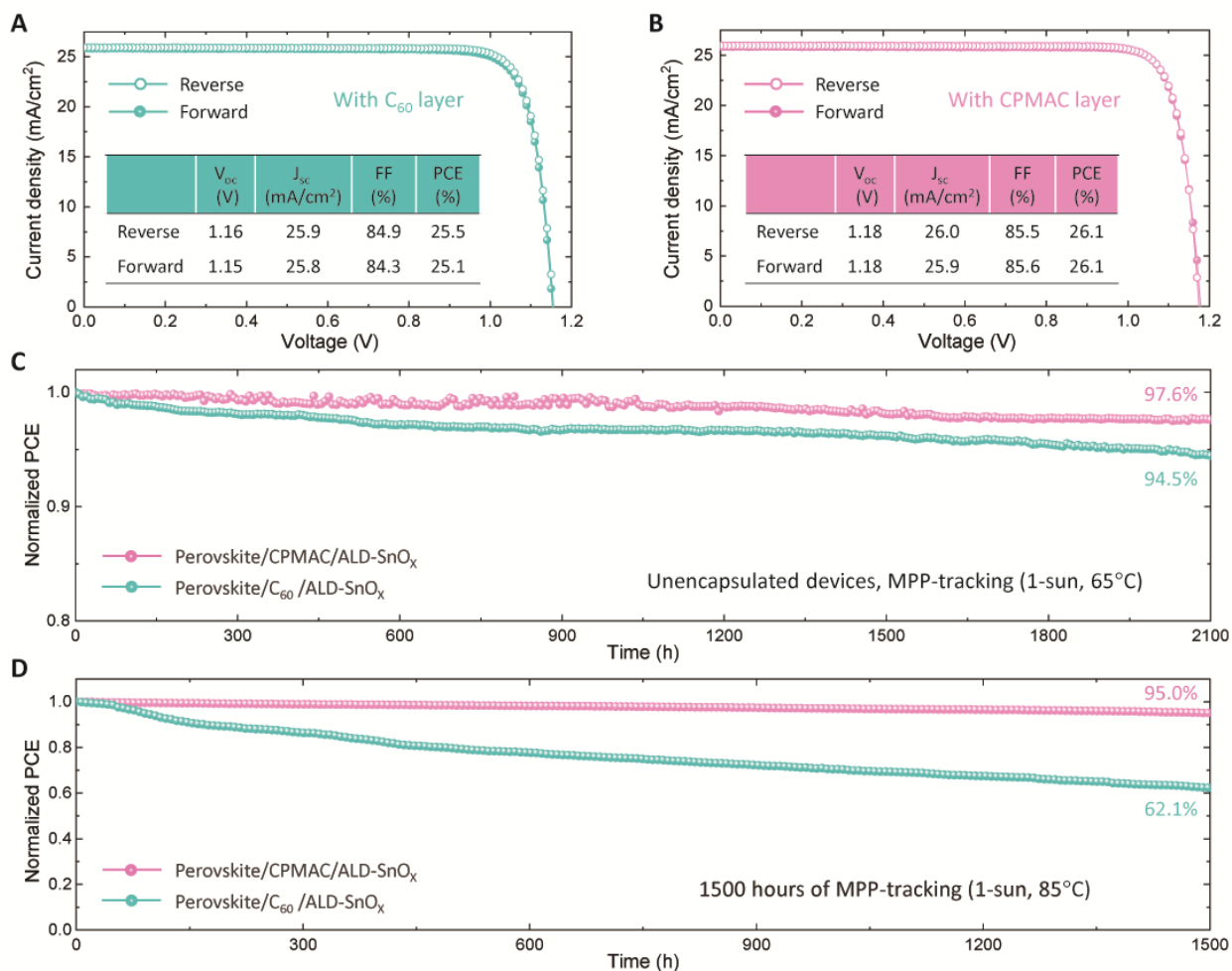


Fig. 3. Perovskite solar cell characteristics. (A) and (B) The current density-voltage (J - V) characteristics of the p-i-n perovskite solar cells with various device configurations (including FTO/HTL/perovskite/C₆₀/ALD-SnO_x/Ag (A) and FTO/HTL/perovskite/CPMAC/ALD-SnO_x/Ag (B), and the corresponding photovoltaic parameters under simulated AM 1.5 G illumination (insets). Device areas were 0.059 cm² as defined by a metal aperture. (C) Comparison of operational stability of devices under 1-sun maximum power point tracking (MPPT) following the ISOS-L-1 protocol (65°C, N₂ atmosphere). HTL was MeO-2PACZ/Me-4PACZ mixture in (A–C). The initial PCEs of C₆₀- and CPMAC-based devices were 24.9% and 25.8%, respectively. (D) Comparison of operational stability of unencapsulated PSCs measured by MPPT under continuous 1-sun illumination (85°C, N₂ atmosphere). For this test, PTAA was used as the HTL. The initial PCEs of C₆₀- and CPMAC-based devices were 24.3% and 25.5%, respectively.

The current density-voltage (J - V) curves and photovoltaic (PV) performance parameters of the champion devices under standard AM 1.5 G illumination are shown in Fig. 3, A and B. The

PSC with the configuration of FTO/HTL/perovskite/ALD-SnO_x/Ag (where FTO is fluorine-doped tin oxide and HTL is hole transport layer) showed a negligible PCE of 0.07% (**fig. S11**), which we ascribed to the degradation of the perovskite layer during the ALD-SnO_x coating (43, 44). The incorporation of a standard C₆₀ layer between perovskite and ALD-SnO_x ameliorated this degradation, achieving a PCE of 25.5% (reverse scan) with a short-circuit current density (J_{sc}) of 26.0 mA cm⁻², open-circuit voltage (V_{oc}) of 1.16 V, and fill factor (FF) of 84.9% (**Fig. 3A**). Remarkably, replacing C₆₀ with CPMAC further improved the PV performance to a PCE of 26.1% (reverse scan) with a J_{sc} of 26.0 mA cm⁻², V_{oc} of 1.18 V, and FF of 85.5% (**Fig. 3B**). The increase in V_{oc} for the CPMAC-based PSC is consistent with its higher photoluminescence quantum yield (PLQY) than the C₆₀-based cell (**fig. S12**). Note that both C₆₀- and CPMAC-based PSCs exhibited minimal hysteresis between forward and reverse J - V scans.

The improved PV parameters achieved by using CPMAC to replace C₆₀ were further verified based on statistical results from 20 devices of each device type (**fig. S13**). The PSCs with the CPMAC layer processed over a range of CPMAC solution concentrations all exhibited similar PCEs (**fig. S14**), which would provide a favorable processing window for solution deposition of the CPMAC layer. Note that the measured J_{sc} (26.0 mA cm⁻²) was consistent with the integrated current density (25.9 mA cm⁻²) from the external quantum efficiency (EQE) spectra (**fig. S15**). It is also noteworthy that CPMAC-based PSCs do not require additional perovskite surface treatment as is often the case for C₆₀-based PSCs (**fig. S16**). The ideality factors (n_{id}) of control and target devices were calculated from the dependence of V_{oc} on the light intensity (**fig. S17**). The n_{id} decreased from 1.77 to 1.41 after substituting the C₆₀ layer with CPMAC, which could be attributed to reduced trap-assisted non-radiative recombination (57, 58).

The operational stability of PSCs with C₆₀ and CPMAC was evaluated to investigate the impact of CPMAC on device stability (**Fig. 3, C and D**). The unencapsulated device with CPMAC exhibited only about a 2% efficiency loss after 2,100 hours of continuous maximum power point tracking (MPPT) under an N₂ atmosphere at about 65°C with 1-sun illumination. In contrast, the C₆₀-based devices showed a ~6% drop in PCE.

We further tested the operational stability at 85°C. For this test, PTAA was used as the HTL as we showed previously the mixed SAM HTL was prone to degradation at 85°C (19). Note that the operational stability at 85°C for the CPMAC-based device was substantially better than the standard C₆₀-based device, maintaining ~95% of its original efficiency over 1,500 hours of MPPT under N₂ (Fig. 3D). When tested under damp-heat conditions (85°C and 85% relative humidity), the encapsulated CPMAC-based device retained 94.3% of its initial PCE after 2,000 hours, whereas the C₆₀-based device exhibited a 16% PCE loss (fig. S18). Thus, replacing C₆₀ with CPMAC increased device stability under various testing conditions. Note that the improved stability with CPMAC is also consistent with the time-of-flight secondary ion mass spectroscopy (ToF-SIMS) measurement of aged PSCs (fig. S19).

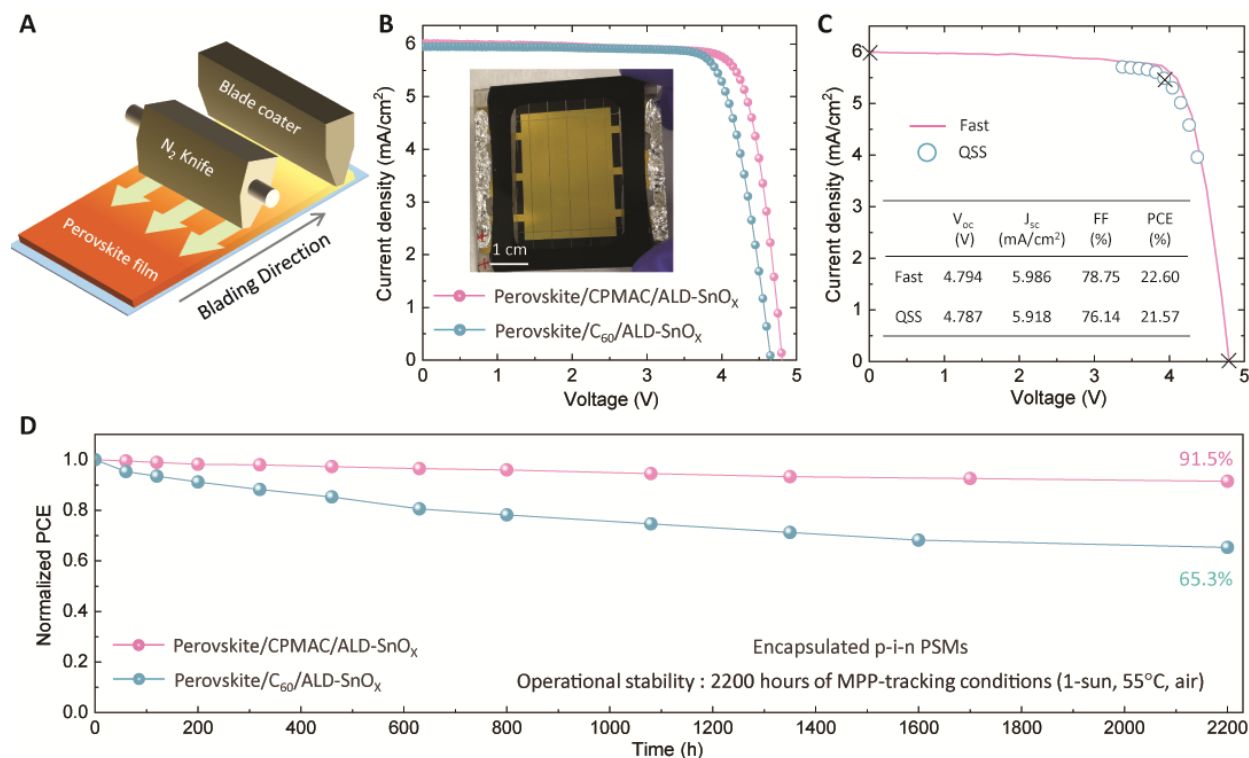


Fig. 4. Perovskite solar module characteristics. (A) Schematic illustration for blade-coating the perovskite films. (B) $J-V$ curves of a representative PSM with C₆₀ and CPMAC (the inset shows a photograph of a typical PSM). (C) Quasi-steady-state (QSS) and $J-V$ results of a representative CPMAC-based device measured by the NREL PV Performance Group. (D) Operational stability of the encapsulated PSMs under 1-sun MPPT following the ISOS-L-1 protocol at ~55°C in air

with 40%–60% relative humidity. The initial PCEs of C₆₀- and CPMAC-based devices were 20.2% and 21.5%, respectively.

Furthermore, we fabricated minimodules with four subcells (6 cm²) by blade-coating the perovskite layer (**Fig. 4A** and **fig. S20**). The representative current density–voltage (*J-V*) curves of perovskite solar minimodules (PSMs) are compared in **Fig. 4B**. The CPMAC-based PSM exhibited a PCE of 23.2% with a J_{sc} of 6.01 mA cm⁻², V_{oc} of 4.81 V, and FF of 80.3%. In comparison, C₆₀-based PSM exhibit a PCE of 21.8%, a V_{oc} of 4.7 V, an FF of 78.6%, and a J_{sc} of 5.95 mA cm⁻². No discernible difference (hysteresis) in *J-V* curves under different scanning directions were observed for the CPMAC-based PSM (**fig. S21**). The corresponding stabilized PCEs of the PSMs based on C₆₀ and CPMAC are 21.2% and 22.7%, respectively (**fig. S22**).

We provided one such device to an accredited PV laboratory (NREL PV Performance Group), obtaining the certified quasi-steady-state (QSS) PCE of 21.6±0.2% with a corresponding backward-scan *J-V* PCE of 22.6% (**figs. S23 and S24 and Fig. 4C**). Importantly, the efficient PSMs with CPMAC on blade-coated perovskite demonstrated that CPMAC could effectively integrate with perovskite processed at scale. We also investigated the operational stability of the encapsulated PSM under continuous light illumination at ~55°C in ambient air (**Fig. 4D**). After 2,200 hours, the CPMAC-treated PSM maintained 91.5% of its initial PCE, whereas the control sample lost >30% of its initial PCE. Our results suggest that using CPMAC to replace C₆₀ is an effective approach to improve the PCE and operational stability of p-i-n PSCs and PSMs.

Discussion

We showed that an ionic salt, CPMAC, can address the mechanical instability associated with the molecular C₆₀ in inverted PSCs. In comparison to C₆₀, the ionic nature associated with CPMAC strengthened the ETL/perovskite interface region. A thin CPMAC layer was sufficient for effective device operation. The use of CPMAC boosted device efficiency and stability. We further demonstrated that CPMAC is suitable for developing minimodules, reaching a PSM efficiency and operational stability that is among the best in the literature. Taken together, our

results point to a promising approach to advance perovskite PV technology toward commercialization.

References

1. Kojima, A., Teshima, K., Shirai, Y. & Miyasaka, T. Organometal Halide Perovskites as Visible-Light Sensitizers for Photovoltaic Cells. *Journal of the American Chemical Society* **131**, 6050-6051 (2009).
2. Yang, Y. et al. Amidination of ligands for chemical and field-effect passivation stabilizes perovskite solar cells. *Science* **386**, 898-902 (2024).
3. Liu, M., Johnston, M.B. & Snaith, H.J. Efficient planar heterojunction perovskite solar cells by vapour deposition. *Nature* **501**, 395-398 (2013).
4. Ding, Y. et al. Cation reactivity inhibits perovskite degradation in efficient and stable solar modules. *Science* **386**, 531-538 (2024).
5. Li, X. et al. Improved performance and stability of perovskite solar cells by crystal crosslinking with alkylphosphonic acid ω -ammonium chlorides. *Nature Chemistry* **7**, 703-711 (2015).
6. Duan, T. et al. Chiral-structured heterointerfaces enable durable perovskite solar cells. *Science* **384**, 878-884 (2024).
7. Abdi-Jalebi, M. et al. Maximizing and stabilizing luminescence from halide perovskites with potassium passivation. *Nature* **555**, 497-501 (2018).
8. Li, Z. et al. Stabilizing Perovskite Structures by Tuning Tolerance Factor: Formation of Formamidinium and Cesium Lead Iodide Solid-State Alloys. *Chemistry of Materials* **28**, 284-292 (2016).
9. Bai, S. et al. Planar perovskite solar cells with long-term stability using ionic liquid additives. *Nature* **571**, 245-250 (2019).
10. He, R. et al. Improving interface quality for 1-cm² all-perovskite tandem solar cells. *Nature* **618**, 80-86 (2023).
11. Zheng, X. et al. Co-deposition of hole-selective contact and absorber for improving the processability of perovskite solar cells. *Nature Energy* **8**, 462-472 (2023).
12. Cheng, Q. et al. Single Crystal Seed Induced Epitaxial Growth Stabilizes α -FAPbI₃ in Perovskite Solar Cells. *Nano Letters* **24**, 5308-5316 (2024).
13. You, S. et al. Multifunctional Polymer-Regulated SnO₂ Nanocrystals Enhance Interface Contact for Efficient and Stable Planar Perovskite Solar Cells. *Advanced Materials* **32**, 2003990 (2020).
14. Luo, L. et al. Stabilization of 3D/2D perovskite heterostructures via inhibition of ion diffusion by cross-linked polymers for solar cells with improved performance. *Nature Energy* **8**, 294-303 (2023).
15. Zhu, H. et al. In situ energetics modulation enables high-efficiency and stable inverted perovskite solar cells. *Nature Photonics* **19**, 28-35 (2025).
16. Xiong, Y. et al. Recent advances in perovskite/Cu(In,Ga)Se₂ tandem solar cells. *Materials*

- Today Electronics* **7**, 100086 (2024).
17. Zhang, S. et al. Grain Boundary and Buried Interface Suturing Enabled by Fullerene Derivatives for High-Performance Perovskite Solar Module. *ACS Energy Letters* **7**, 3958-3966 (2022).
 18. Chen, M. et al. Stress Engineering for Mitigating Thermal Cycling Fatigue in Perovskite Photovoltaics. *ACS Energy Letters* **9**, 2582-2589 (2024).
 19. Jiang, Q. et al. Towards linking lab and field lifetimes of perovskite solar cells. *Nature* **623**, 313-318 (2023).
 20. Fei, C. et al. Strong-bonding hole-transport layers reduce ultraviolet degradation of perovskite solar cells. *Science* **384**, 1126-1134 (2024).
 21. Lin, R. et al. All-perovskite tandem solar cells with 3D/3D bilayer perovskite heterojunction. *Nature* **620**, 994-1000 (2023).
 22. Jiang, Q. & Zhu, K. Rapid advances enabling high-performance inverted perovskite solar cells. *Nature Reviews Materials* **9**, 399-419 (2024).
 23. Wang, H. et al. Impurity-healing interface engineering for efficient perovskite submodules. *Nature* **634**, 1091-1095 (2024).
 24. Zhu, P. et al. Aqueous synthesis of perovskite precursors for highly efficient perovskite solar cells. *Science* **383**, 524-531 (2024).
 25. Gao, H. et al. Homogeneous crystallization and buried interface passivation for perovskite tandem solar modules. *Science* **383**, 855-859 (2024).
 26. Park, S.M. et al. Engineering ligand reactivity enables high-temperature operation of stable perovskite solar cells. *Science* **381**, 209-215 (2023).
 27. Chen, Y. et al. Nuclei engineering for even halide distribution in stable perovskite/silicon tandem solar cells. *Science* **385**, 554-560 (2024).
 28. Tang, X. et al. Reconstruction of Electron-Selective Interface via Multifunctional Chemical Bridging Enables High-Performance Rigid and Flexible Perovskite Solar Cells. *ACS Energy Letters* **9**, 5679-5687 (2024).
 29. You, S. et al. A Biopolymer Heparin Sodium Interlayer Anchoring TiO₂ and MAPbI₃ Enhances Trap Passivation and Device Stability in Perovskite Solar Cells. *Advanced Materials* **30**, 1706924 (2018).
 30. Dong, B. et al. Self-assembled bilayer for perovskite solar cells with improved tolerance against thermal stresses. *Nature Energy* (2025).
 31. Liu, X. et al. Mesoscale Ordering 3D Mosaic Self-Assembly of Dopant-Free Hole Transport Material for Perovskite Solar Cells. *ACS Energy Letters* **9**, 2446-2455 (2024).
 32. Chen, J. et al. Efficient tin-based perovskite solar cells with trans-isomeric fulleropyrrolidine additives. *Nature Photonics* **18**, 464-470 (2024).
 33. Shi, P. et al. Oriented nucleation in formamidinium perovskite for photovoltaics. *Nature* **620**, 323-327 (2023).
 34. Park, J. et al. Controlled growth of perovskite layers with volatile alkylammonium chlorides. *Nature* **616**, 724-730 (2023).
 35. Jeon, N.J. et al. Compositional engineering of perovskite materials for high-performance

- solar cells. *Nature* **517**, 476-480 (2015).
36. Luo, D. et al. Enhanced photovoltage for inverted planar heterojunction perovskite solar cells. *Science* **360**, 1442-1446 (2018).
 37. Lin, Y.-H. et al. A piperidinium salt stabilizes efficient metal-halide perovskite solar cells. *Science* **369**, 96-102 (2020).
 38. Pont, S., Foglia, F., Higgins, A.M., Durrant, J.R. & Cabral, J.T. Stability of Polymer:PCBM Thin Films under Competitive Illumination and Thermal Stress. *Advanced Functional Materials* **28**, 1802520 (2018).
 39. Distler, A. et al. The Effect of PCBM Dimerization on the Performance of Bulk Heterojunction Solar Cells. *Advanced Energy Materials* **4**, 1300693 (2014).
 40. Shen, W. et al. A Crystalline 2D Fullerene-Based Metal Halide Semiconductor for Efficient and Stable Ideal-bandgap Perovskite Solar Cells. *Advanced Energy Materials* **14**, 2400582 (2024).
 41. Warby, J. et al. Understanding Performance Limiting Interfacial Recombination in pin Perovskite Solar Cells. *Advanced Energy Materials* **12**, 2103567 (2022).
 42. Stolterfoht, M. et al. Visualization and suppression of interfacial recombination for high-efficiency large-area pin perovskite solar cells. *Nature Energy* **3**, 847-854 (2018).
 43. Hultqvist, A. et al. SnOx Atomic Layer Deposition on Bare Perovskite—An Investigation of Initial Growth Dynamics, Interface Chemistry, and Solar Cell Performance. *ACS Applied Energy Materials* **4**, 510-522 (2021).
 44. Palmstrom, A.F. et al. Interfacial Effects of Tin Oxide Atomic Layer Deposition in Metal Halide Perovskite Photovoltaics. *Advanced Energy Materials* **8**, 1800591 (2018).
 45. Johnson, S.A. et al. Improving the barrier properties of tin oxide in metal halide perovskite solar cells using ozone to enhance nucleation. *Joule* **7**, 2873-2893 (2023).
 46. Liu, C. et al. Bimolecularly passivated interface enables efficient and stable inverted perovskite solar cells. *Science* **382**, 810-815 (2023).
 47. Azmi, R. et al. Double-side 2D/3D heterojunctions for inverted perovskite solar cells. *Nature* **628**, 93-98 (2024).
 48. Li, C. et al. Diamine chelates for increased stability in mixed Sn–Pb and all-perovskite tandem solar cells. *Nature Energy* **9**, 1388-1396 (2024).
 49. Li, X. et al. Constructing heterojunctions by surface sulfidation for efficient inverted perovskite solar cells. *Science* **375**, 434-437 (2022).
 50. Zhao, J. et al. Suppressed Defects by Functional Thermally Cross-Linked Fullerene for High-Efficiency Tin-Lead Perovskite Solar Cells. *Advanced Materials* **36**, 2406246 (2024).
 51. Doherty, T.A.S. et al. Performance-limiting nanoscale trap clusters at grain junctions in halide perovskites. *Nature* **580**, 360-366 (2020).
 52. Chen, P. et al. In Situ Growth of 2D Perovskite Capping Layer for Stable and Efficient Perovskite Solar Cells. *Advanced Functional Materials* **28**, 1706923 (2018).
 53. Stranks, S.D. Nonradiative Losses in Metal Halide Perovskites. *ACS Energy Letters* **2**, 1515-1525 (2017).
 54. You, S. et al. Bifunctional hole-shuttle molecule for improved interfacial energy level

- alignment and defect passivation in perovskite solar cells. *Nature Energy* **8**, 515-525 (2023).
55. Dai, Z. et al. Connecting Interfacial Mechanical Adhesion, Efficiency, and Operational Stability in High Performance Inverted Perovskite Solar Cells. *ACS Energy Letters* **9**, 1880-1887 (2024).
 56. Casareto, M. & Rolston, N. Designing metal halide perovskite solar modules for thermomechanical reliability. *Communications Materials* **5**, 74 (2024).
 57. Kim, M. et al. Conformal quantum dot-SnO₂ layers as electron transporters for efficient perovskite solar cells. *Science* **375**, 302-306 (2022).
 58. Jeong, J. et al. Pseudo-halide anion engineering for α -FAPbI₃ perovskite solar cells. *Nature* **592**, 381-385 (2021).
 59. Jiang, Q. et al. Compositional texture engineering for highly stable wide-bandgap perovskite solar cells. *Science* **378**, 1295-1300 (2022).
 60. Mollón, V., Bonhomme, J., Viña, J. & Argüelles, A. Mixed mode fracture toughness: An empirical formulation for GI/GII determination in asymmetric DCB specimens. *Engineering Structures* **32**, 3699-3703 (2010).
 61. Li, M. et al. Strategies to improve the mechanical robustness of metal halide perovskite solar cells. *Energy Advances* **3**, 273-280 (2024).
 62. Reid, O.G. et al. Quantitative analysis of time-resolved microwave conductivity data. *Journal of Physics D: Applied Physics* **50**, 493002 (2017).
 63. Kresse, G. & Furthmüller, J. Efficient iterative schemes for ab initio total-energy calculations using a plane-wave basis set. *Physical Review B* **54**, 11169-11186 (1996).
 64. Kresse, G. & Furthmüller, J. Efficiency of ab-initio total energy calculations for metals and semiconductors using a plane-wave basis set. *Computational Materials Science* **6**, 15-50 (1996).
 65. Blöchl, P.E. Projector augmented-wave method. *Physical review B* **50**, 17953 (1994).
 66. Perdew, J.P., Burke, K. & Ernzerhof, M. Generalized Gradient Approximation Made Simple. *Physical Review Letters* **77**, 3865-3868 (1996).
 67. Grimme, S., Antony, J., Ehrlich, S. & Krieg, H. A consistent and accurate ab initio parametrization of density functional dispersion correction (DFT-D) for the 94 elements H-Pu. *The Journal of Chemical Physics* **132** (2010).
 68. Jeong, J. et al. Carbazole Treated Waterproof Perovskite Films with Improved Solar Cell Performance. *Advanced Energy Materials* **15**, 2401965 (2025).

Acknowledgments

Funding: The work was authored in part by the National Renewable Energy Laboratory, operated by Alliance for Sustainable Energy, LLC, for the U.S. Department of Energy (DOE) under contract no. DE-AC36-08GO28308. We acknowledge the support on molecule design, first-principles calculations, and transient spectroscopy measurements from the Center for Hybrid Organic-

Inorganic Semiconductors for Energy (CHOISE), an Energy Frontier Research Center funded by the Office of Basic Energy Sciences, Office of Science within the U.S. Department of Energy. The DFT calculations were performed using computational resources sponsored by the U.S. Department of Energy's Office of Energy Efficiency and Renewable Energy and located at the National Renewable Energy Laboratory, and the resources of the National Energy Research Scientific Computing Center (NERSC), a U.S. Department of Energy Office of Science User Facility located at Lawrence Berkeley National Laboratory, operated under Contract No. DE-AC02-05CH11231 using NERSC award BES-ERCAP0032847. We also acknowledge the support on module development from DE-FOA-0002064 and award number DE-EE0008790, the support on the general perovskite fabrication and characterization from the Perovskite Enabled Tandems program, funded by the U.S. Department of Energy, Office of Energy Efficiency and Renewable Energy, Solar Energy Technologies Office Award Number 52776, and the support on the mechanical testing from the National Science Foundation under Grant No. 2339233. M.F. and Z.S. acknowledge the support on CPMAC synthesis by the Royal Society through the University Research Fellowship (URF/R1/191286), Research Grant 2021 (RGS/R1/211321), and UKRI EPSRC Standard Grant EP/WO25280/1. The views expressed in the article do not necessarily represent the views of the DOE or the U.S. Government. The U.S. Government retains and the publisher, by accepting the article for publication, acknowledges that the U.S. Government retains a nonexclusive, paid-up, irrevocable, worldwide license to publish or reproduce the published form of this work, or allow others to do so, for U.S. Government purposes. **Author Contributions:** S.Y. and K.Z. conceived the idea. K.Z., O.M.B., M.F., and Y.Yan. supervised the projects and process. S.Y., Z.S., and H.Z. conceptualized and designed the experiments. S.Y. and H.Z. fabricated perovskite solar cells and conducted device efficiency and stability measurements. Z.S. prepared the CPMAC and conducted NMR measurements. X.W. carried out the DFT calculation under the supervision of Y.Yan. B.S. and J.L. conducted the PL mapping measurement and other PL measurements. Q.W. conducted the cryo-TEM measurement. Y.Yuan conducted the GIWAXS measurement. B.D.D., E.M.S., T.R., and A.L. provided support on module fabrication and

packaging. Y.D. conducted TRMC measurements and analysis under the guidance of M.C.B. M.C. conducted the mechanical measurement and analysis under the guidance of N.R. J.J.B. provided valuable suggestions for experiment planning, analysis, and manuscript preparation. S.Y., H.Z., Z.S., O.M.B., Y.Yan, and K.Z. wrote the manuscript. All authors discussed the results and contributed to the revisions of the manuscript. **Competing interests:** S.Y., Z.S., M.F., and K.Z. are inventors on a provisional patent (US patent application number No. 63/669,821) related to the subject matter of this manuscript. **Data and materials availability:** All data needed to evaluate the conclusions in the paper are present in the paper or the Supplementary Materials.

SUPPLEMENTARY MATERIALS

Materials and Methods

Figs. S1 to S24

References (59-68)